

PAPER • OPEN ACCESS

Optimization of ion transport in a combined RFQ Cooler with axial magnetic field

To cite this article: M. Cavenago *et al* 2022 *J. Phys.: Conf. Ser.* **2244** 012064

View the [article online](#) for updates and enhancements.

You may also like

- [Deuteron beam commissioning of the linear IFMIF prototype accelerator ion source and low energy beam transport](#)
N. Chauvin, T. Akagi, L. Bellan *et al.*
- [CW RFQ design and investigation for multi-charge-state acceleration of radioactive beams from BISOL](#)
P.P. Gan, H.P. Li, Z. Wang *et al.*
- [Design study of a radio-frequency quadrupole for high-intensity beams](#)
Jungbae Bahng, Eun-San Kim and Bong-Hyuk Choi



The Electrochemical Society
Advancing solid state & electrochemical science & technology

241st ECS Meeting

Vancouver, BC, Canada. May 29 – June 2, 2022

ECS Plenary Lecture featuring
Prof. Jeff Dahn,
Dalhousie University

Register now!

The banner features the ECS logo, a 'Register now!' button with a checkmark, and a photograph of Prof. Jeff Dahn pointing at a whiteboard. The background of the banner shows the Science World geodesic dome in Vancouver, BC, Canada, with a waterfront view and buildings in the distance.

Optimization of ion transport in a combined RFQ Cooler with axial magnetic field

M. Cavenago¹, M. Romé², G. Maero², L. Bellan¹, F. Cavaliere², M. Comunian¹, A. Galatà¹, M. Maggiore¹, N. Panzeri², A. Pisent¹, L. Pranovi¹, M. Sattin¹

¹ INFN-Laboratori Nazionali di Legnaro, Legnaro, IT

² University of Milano, Dip Fisica, e INFN-MI, Milano, IT

E-mail: cavenago@lnl.infn.it

Abstract. The accurate mass spectrometry (with resolution goal 1:20000) of exotic ions requests beams with low energy spread (goal is about 0.5 eVrms or lower) and low transverse emittance, so it is necessary to cool ions produced by a fission source. In a radiofrequency (rf) quadrupole cooler (RFQC), collisions decrease ion kinetic energy, while rf and DC voltages confine and reaccelerate ions towards the extraction, where the cold ion beam is formed. Operation is based on carefully chosen tunings of voltages and of gas pressure p_g , which requires an adequate pumping system; efficient simulations of extraction systems, which critically depend on residual speed of ions, are also important. Progresses in the experimental setup are described. Indications from simple ray tracing and 'ray+collision' tracing are compared. Results are applied to a simple triode extraction system, and more flexible configurations are considered.

1. Introduction

Radio Frequency Quadrupole Coolers (RFQC) are a typical part of facilities for reacceleration of beams produced by fission targets, as in the SPES (Selective Production of Exotic Species[1]) project at LNL. Cooling is obtained by collisions of ions with a gas[2, 3] as Helium, while confinement is due to a radiofrequency (rf) field, which gives focusing, but also introduces an heating effect. Additional confinement may be provided with a solenoidal magnetic field \mathbf{B}^s , so that rf amplitude voltage V_{rf} can be reduced and ion transmission improved; an RFQC prototype built at LNL[4] has reduced dimensions (length $L_1 = 0.72$ m, outer diameter $\cong 0.15$ m), so it can be inserted in the Eltrap facility at Milan University[5], a $L_0 \cong 1.6$ m long solenoid, with a 0.25 m inner diameter vacuum chamber (see Fig. 1). Indeed, the required optimization of transmission, transverse cooling and longitudinal cooling is challenging[6, 7] and up to now calculations are based on many simplifying assumptions, here discussed in section III, so that experimental tests are necessary also to validate calculations. Set-up, whose status is reported in section II, also integrates an emittance meter EMI1, two Faraday cups FC1 and FC2, a commercial ion source IS1 for initial tests, and the gas differential pumping of RFQC.

Due the quadrupole pattern of electrodes and since wavelength $2\pi c/\omega$ is much larger than r_0 , half distance between facing electrodes (see fig 2.a), inside RFQC the rf field is $\mathbf{E}_f = -\nabla\phi_f$ with an electric potential $\phi_f \cong 2V_{rf}(xy/r_0^2) \cos\omega t$ near z axis; in our case $\omega \cong 2.5 \times 10^7$ rad/s (about 4 MHz). The RFQC is divided in N sections by gaps (Fig. 2.b and 2.c); we have $4*N$



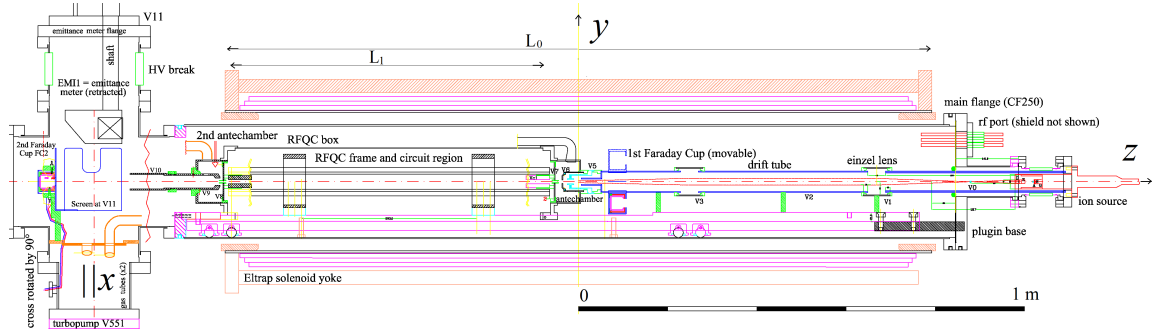


Figure 1. Eltrap+RFQC setup; see Figs 2,3 of Ref [7] and Fig 1 of Ref [11] for details.

electrodes, which can be biased to different static potentials $\phi_s = V_n^c$ (with $n = 1, \dots, 10$), so to add a static field $\mathbf{E}_s = -\nabla\phi_s$.

Ions are singly charged with atomic number $A \leq 133$; kinetic energy K_i is typically 40 keV in our accelerator applications; our IS1 provides a maximum of $K_i = 5$ keV, with voltages quoted here adjusted for this case. The accurate mass spectrometry (with resolution goal 1:20000) of exotic ions requests beam with low energy spread (goal is ≤ 0.5 eVrms, while exotic ion source gives few eVrms spread) and low transverse geometrical emittance: we need $\epsilon_{geo} < 7$ mm-mrad for the beam exiting the RFQC with $K_i = 5$ keV, with input $\epsilon_{geo}^i \cong 24$ mm-mrad (or equivalently $\epsilon_{geo} < 2.4$ mm-mrad and $\epsilon_{geo}^i \cong 9$ mm-mrad with $K_i = 40$ keV[1, 8]). The so-necessary ion cooling requires several steps: 1) the injection, where the beam is focused to enter the RFQC, well between electrodes ($r_0 \cong 4.5$ mm in our case), and decelerated to $K_i \leq 0.1$ keV, so that collisions are more effective[9] and transit time longer; 2) transit in the RFQC, where collisions decrease ion kinetic energy, while rf and solenoid fields confine ions, and the bias potential ϕ_s (between RFQC sections) pushes ions towards the extraction; 3) extraction, where the cold ion beam is formed and accelerated again. This is critical since the beam size and velocity depends on previous steps, and reacceleration overfocusing must be controlled. We consider triode systems for extraction, while different solutions (microRFQ[10], tetrode) exist.

2. Setup

RFQC integration in the Eltrap test facility is shown in Fig. 1; the alkali metal ion source IS1, the injection line, the RFQC and its extraction line, are mounted on a rigid 2 m long plugin, which can be assembled, cabled, aligned, and tested outside, and then inserted inside the Eltrap vacuum chamber. Plugin support is a machined Al bar joined to a CF250/CF63 transition and a CF63 flanged isolator where IS1 is mounted. Let z be the solenoid axis, with origin at the



Figure 2. (a) xy section of RFQC; for symmetry, electrostatic simulation reduces to one-quarter geometry; (b) end of RFQC, showing the last two sections of electrodes and the support; (c) 3D geometry of a section of RFQC, showing the gap between electrodes.

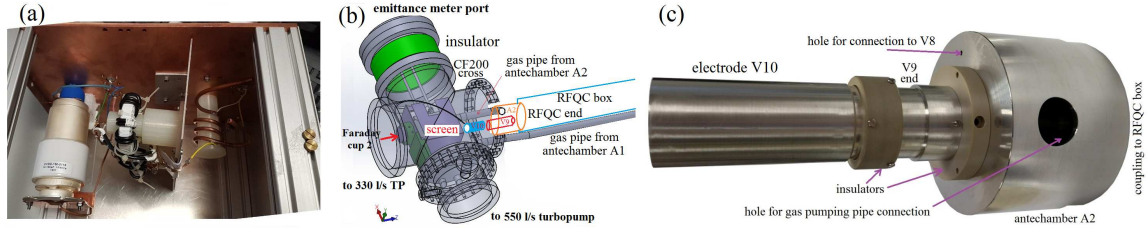


Figure 3. (a) matching box; (b) scheme of EMI1 and pumps; (c) view of triode extraction line

solenoid middle; ion source IS1 cathode is placed at $z_c = 1.021$ m, with its exit lens at $z_e = 0.996$ m; beam is directed towards negative z and exit lens produces a waist at $z_w = 0.85$ m (spot radius 0.5 mm, divergence 4 mrad). Ion beam propagates inside drift tubes V0 (joined to IS1 exit tube), V2, V4 held at say $V_0 = -4.8$ kV respect to ground, so that source cathode is at potential $V_s = K_i/e + V_0 = 200$ V, which can be precisely measured. Ion beam is refocused by einzel lens V1 and V3, and electrodes V5 and V6 decelerate it[11]. A Faraday cup FC1 can be inserted or removed inside drift tube V4.

The RFQC is enclosed in a gas tight box (-0.8 m $< z < -0.05$ m), at ground, except for the end plates V_7 and V_8 (within 100 V from ground). Extraction triode is formed by this plate V_8 , an electrode V_9 (partly inside an antechamber A2) and a drift tube V_{10} ; beam may finally reach the pepper pot emittance meter EMI1 or second Faraday cup FC2. The movable emittance meter EMI1 is mounted on a 40 kV ceramic break (with axis $z = -1.085$ m plane) on a CF200 cross (with gas pumping). Beam image is formed on the EMI1 scintillating screen at $z = -1.055$ m and reflected to a camera. Current of Cs^+ ions is limited to $I_i \leq 200$ nA when the emittance meter is used. In principle FC2 can measure energy spread provided its gate voltage V_g is stable enough; stability $V_g - V_s$ within 0.1 Vpp is necessary, with electronics in development. Other critical equipment, IS1 and EMI1 were fully tested in a separated bench.

The matching box (Fig 3.a) splits the rf input power into two signals V_{rf1} , V_{rf2} , matched to capacitive loads about 200 pF, in phase opposition $V_{rf1} = -V_{rf2}$; RFQC electrodes are connected by capacitors to these signals and by resistors to the bias voltages V_n^c ; this network is placed in the RFQC box, on a thermal sink (a copper bar with mica washers).

Differential gas pumping is needed[12]: inside RFQC a pressure $p_g = 2$ to 9 Pa must be provided, while we prefer $p < 0.001$ Pa in beamline and near EMI1; so RFQC box beam holes are restricted below 3 mm diameter and face antechambers A1 and A2, differentially pumped by 20 mm pipes (fig. 3.b); shaping these pipes to reach the V551 turbopump proved laborious. Two smaller pipes connects the RFQC box to the CF250 plugin flange: one connects to a capacitive p_g meter, the other is the gas input, operated with a small duty cycle (to save He). Most parts were acquired and tested, even if final assembly was delayed by emergency situation.

3. Ion transport and simulations

Let e and m_i be the ion charge and mass, and m_t the gas molecule mass. Due to rf field, each ion trajectory oscillates with angular frequency ω (micromotion) around an average trajectory $\mathbf{x}(t)$ (macromotion [13], driven by the so-called ponderomotive force $\mathbf{F}_p \equiv e\mathbf{E}_p = -e\nabla\phi_p$ with ϕ_p ponderomotive potential). The basic results for macromotion and friction force \mathbf{F}_r due to gas collision was detailed elsewhere[2, 7, 11], with $\phi_p \cong (m_i/2e)\omega_M^2(x^2 + y^2)$ and $F_r = -m_i\nu\nu_m$ where ν_m is the collision frequency (depending on gas density n_g and on macromotion velocity $\mathbf{v} = d_t\mathbf{x}$, see Fig. 4 in Ref[7]). Macromotion frequency ω_M and cyclotron frequency Ω_i are

$$\omega_M = \frac{e}{m_i\sqrt{2}} \frac{V_{rf}}{\omega r_0^2}, \quad \Omega_i = \frac{e|B^s|}{m_i} \quad (1)$$

A convenient parameter of rf strength is $V_p = (m_i/2e)\omega_M^2 r_0^2$; simulations are simplified by axial symmetry of ϕ_p (2D3V) and of other beamline components (einzel lens, the triode, the ion source and the solenoid); $H_i = eV_s$ is value of energy $H = K_i + e\phi$ at ion source. Since $m_i/m_t \gg 1$, many gas collisions are needed to change \mathbf{v} significantly; 1st order effect is the friction force given above, 2nd order effect is a straggling, which can be modeled by a Langevin-style equation:

$$d_t \mathbf{v} = \frac{e}{m_i} (\mathbf{E}_s + \mathbf{E}_p + \mathbf{v} \times \mathbf{B}^s) - \nu_m \mathbf{v} + \boldsymbol{\eta} \quad , \quad \langle \boldsymbol{\eta} \rangle = 0 \quad , \quad \langle \eta^m(t) \eta^n(t') \rangle = D^{mn} \delta(t - t') \quad (2)$$

where $\langle \rangle$ indicates the statistical average, $\boldsymbol{\eta}$ is a random kick, with 2nd order moment given by diffusion tensor D , and $m, n = 1, 2, 3$ or x, y, z are coordinate indexes. A method[14] to simply account for D is summarized as follows. In paraxial approximation $v_x, v_y \ll |v_z|$, and the D non-zero components are $D^{xx} = D^{yy}$ and D^{zz} , calculated from interatomic potential, in the same way as the mobility and collision frequency[2, 7]. Let $\bar{x} = \langle x \rangle$; then $\tilde{x} = x - \bar{x}$ is the random fluctuation around the ray \bar{x} , computed with ray-tracing as usual. For the 2nd moments of the fluctuation, defined as

$$a_{mn} = \langle \tilde{x}^m \tilde{x}^n \rangle \quad , \quad b_{mn} = \langle \tilde{v}^m \tilde{v}^n \rangle \quad , \quad c_{mn} = \langle \tilde{x}^m \tilde{v}^n \rangle \quad , \quad (3)$$

time evolution follows from eq. 2 linearized around \bar{x} and from symmetries. In our case (paraxial approximation) the non-zero independent components are not only a_{zz}, b_{zz}, c_{zz} , and $a_{xx} = a_{yy}, b_{xx} = b_{yy}$ and $c_{xx} = c_{yy}$ as trivially expected, but also $c_{xy} = -c_{yx}$ due to solenoid field (a total of 7 quantities out of 21 components). For example

$$d_t a_{xx} = 2c_{xx} \quad , \quad d_t c_{xy} = -\Omega_i c_{xx} - \nu_m c_{xy} \quad , \quad d_t b_{xx} = 2(D^{xx} - \nu_m b_{xx} - \psi_{,xx} c_{xx}) \quad (4)$$

with $\psi = e(\phi_s + \phi_p)/m_i$ and similarly for others. The pencil emittance, defined by

$$\epsilon_x^p = \sqrt{a_{xx} b_{xx} - c_{xx}^2 - c_{xy}^2} \quad \rightarrow \quad d_t (\epsilon_x^p)^2 = 2a_{xx} D^{xx} - 2\nu_m (\epsilon_x^p)^2 \quad , \quad (5)$$

is constant where gas is absent (where D^{xx} and ν_m are zero). Evolution of reduced Hamiltonian $h = H/m_i = \frac{1}{2} \mathbf{v}^2 + (e\phi_s/m_i)$ and its fluctuation 2nd momentum $b_{hh} = \langle (\dot{h})^2 \rangle$ are also computed.

Simulation results shown in Figs 4 and 5 refer to standard tuning of RFQC; $B_z = 0.11$ T, $V_p = 1.95$ V, injection energy $H_i = 200$ eV or $H_i = 200 \pm 5$ eV, and n -th section bias voltage $V_n^c = (11 - n)V_o$ with $V_o = 10$ V; both gas pressure p_g inside RFQC (from 2 to 9 Pa) and triode lens voltage V_9 were scanned. First note in Fig. 4.a (from ray-tracing with different H_i) that final average energy H_a differs at most by 1 eV for $p_g = 2$ Pa and is negligible for $p_g = 9$ Pa. On the other hand (Fig. 4.b), the rms contribution of fluctuation (or diffusion) roughly changes

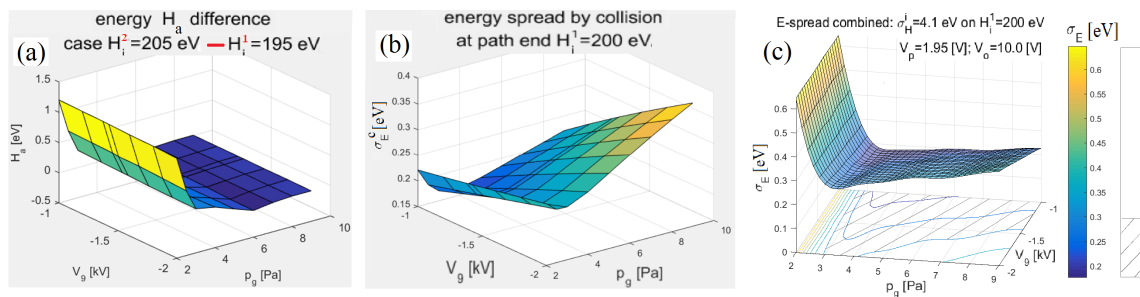


Figure 4. (a) difference of average final energies H_a vs gas pressure p_g and lens voltage V_9 for two H_i ; (b) rms fluctuation induced by gas collisions; (c) combined rms energy spread.

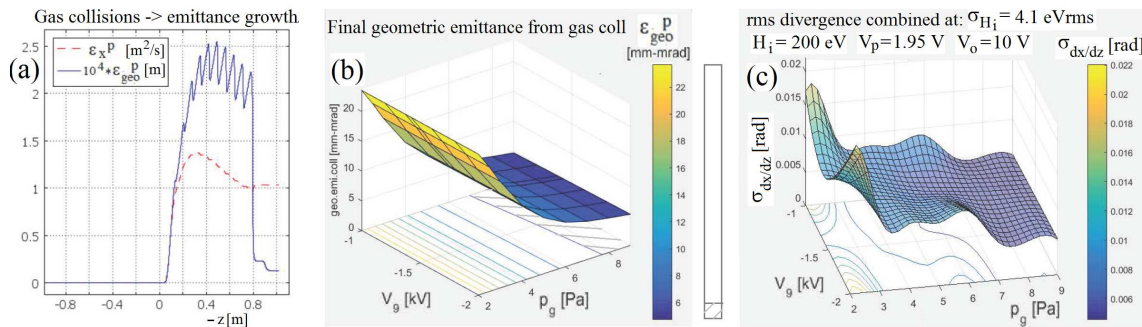


Figure 5. (a) pencil emittance ϵ_x^p vs $-z$; growth and damping due to gas collisions with $p_g = 4$ Pa; also plotted rms ϵ_{geo}^p ; (b) output value of ϵ_{geo}^p ; (c) output value of rms divergence.

as p_g . Relative weight of these effects depends from input energy spread σ_{H_i} (that is about 0.1 eV for IS1 and is expected ≥ 4 eV in exotic beam application[1, 8]). Assuming $\sigma_{H_i} \cong 4$ eV gives Fig. 4.c result, with a wide optimum plateau (from 3 to 9 Pa) for the output energy spread σ_E , which includes shown effects and also minor terms due to beam size; hatched region is $\sigma_E < 0.3$ eVrms. To mimic $\sigma_{H_i} \cong 4$ eV in Eltrap installation, we simply sum results at several H_i , for example at 195, 200 and 205 eV.

The pencil emittance is shown in fig 5.a for $H_i = 200$ eV (note $-z$ abscissa to follow beam direction); initial value is zero (no fluctuation) until gas region is met; emittance reaches roughly a value $(a_{xx} D^{xx} / \nu_m)^{1/2}$ slowly decreasing (since K_i is decreasing) until the RFQC exit is reached, after which ϵ_x^p is frozen. Evolution of pencil geometric emittance $\epsilon_{geo}^p \equiv \epsilon_x^p / |v_z|$ reveals more features: passing from one section to the other, each ion is accelerated (by bias voltage drop) in a $2r_0$ distance[7], so ϵ_{geo}^p has sharp repeated decreases; finally after RFQC exit we see a final decrease, due to the large reacceleration. A scan of output ϵ_{geo}^p in fig 5.b simply reveals a decrease with p_g (good region $\epsilon_{geo}^p < 6$ mm-mrad is hatched). A preliminary result for rms total divergence is shown in fig. 5.c; note that the $V_g \cong -1.4$ kV optimum shows up, with a preferred trend for large $p_g \cong 9$ Pa.

Experimental tests of emittance ϵ_{geo} are expected in the beginning of 2022, while σ_E measurements request more time. Extraction tests with more electrodes (tetrode and so on) are envisioned through 2023, also to investigate a better balance of ϵ_{geo} and σ_E cooling and p_g effects.

Acknowledgments

Work set up in collaboration and financial support of INFN-Group 5.

- [1] Comunian M et al. 2020 *J. Phys. Conf. Ser.* **1401** 012002.
- [2] Schwarz S 2006 *Nucl. Instrum. Meth.* **A 566** 233.
- [3] Herfurth F et al. 2001 *Nucl. Instrum. Meth. Phys. Research* **A469** 254.
- [4] Maggiore M et al. 2014 *Rev. Sci. Instrum.* **85** 02B909; doi: 10.1063/1.4830357
- [5] Amoretti M. et al. 2003 *Rev. Sci. Instrum.* **74** 3991.
- [6] Guo-Zhong Li and Werth G 1992 *Phys. Scr.* **46** 587.
- [7] Cavenago M et al. 2019 *Rev. Sci. Instrum* **91** 113324.
- [8] Comunian M et al. 2018 *9th Int. Particle Acc. Conf., IPAC18* pp 3252-3254, online at www.jacow.org.
- [9] Lieberman M A and Lichtenberg A J 1994 *Principles of Plasma Discharges and Material Processing*, John Wiley, New York, especially chapter 4.
- [10] Boussaid R, Ban G, Quémérer G, Merrer Y and Lorry J 2017 *Phys. Rev., ST-AB* **20** 124701.
- [11] Cavenago M et al. 2016 *Rev. Sci. Instrum.* **87** 02B504.
- [12] Barquest B R et al. 2018 *9th Int. Particle Acc. Conf., IPAC18*, pp 3914-3916; online at www.jacow.org.
- [13] Moore R B, Gianfrancesco O, Lumbo R and Schwarz S 2006 *Int. J. Mass Spectr.* **251** 190.
- [14] Cavenago M, unpublished.